Observation of a phononic quadrupole topological insulator

Marc Serra-Garcia,[1, *] Valerio Peri,[1, *] Roman Süsstrunk,[1] Osama R. Bilal,[1, 2] Tom Larsen,[3] Luis Guillermo Villanueva,[3] and Sebastian D. Huber[1]

[1]*Institute for Theoretical Physics, ETH Zurich, 8093 Zürich, Switzerland*
[2]*Division of Engineering and Applied Science, California Institute of Technology, Pasadena, CA 91125, USA*
[3]*Advanced NEMS Group, École Polytechnique Fédérale de Lausanne (EPFL), 1015 Lausanne, Switzerland*
(Dated: August 18, 2017)

The modern theory of charge polarization in solids is based on a generalization of Berry's phase. Its quantization lies at the heart of our understanding of all systems with topological band structures that were discovered over the last decades. These include the quantum Hall effect, time-reversal invariant topological insulators in two and three dimensions as well as Weyl semi-metals. Recently, the theory of this quantized polarization was extended from the dipole- to higher multipole-moments [1]. In particular, a two-dimensional quantized quadrupole insulator is predicted to have gapped yet topological one-dimensional edge-modes, which in turn stabilize zero-dimensional in-gap corner states. However, such a state of matter has not been observed experimentally. Here, we provide the first measurements of a phononic quadrupole insulator. We experimentally characterize the bulk, edge, and corner physics of a mechanical metamaterial and find the predicted gapped edge and in-gap corner states. We further corroborate our findings by comparing the mechanical properties of a topologically non-trivial system to samples in other phases predicted by the quadrupole theory. From an application point of view, these topological corner states are an important stepping stone on the way to topologically protected wave-guides in higher dimensions and thereby open a new design path for metamaterials.

A non-vanishing dipole moment $\mathbf{p} = \langle \Psi | \mathbf{r} | \Psi \rangle$ in an insulator[2,3] does not lead to any charge accumulation in the bulk. However, it manifests itself through uncompensated surface charges and hence induces potentially interesting surface physics, see Fig. 1a. The dipole moment $\mathbf{p}$ is expressible through Berry's phase,[2,4] which in turn can lead to its quantization.[5–15] All observed topological insulators fit into this framework of quantized dipole moments,[6] or mathematical generalizations thereof.[12] Whether higher order moments of the electronic charge distribution, such as the quadrupole moment, can lead to distinctly new topological phases of matter remained unclear.

Recently, a theory for a quantized quadrupole insulator was put forward[1] based on its phenomenology: A bulk quadrupole moment in a finite two-dimensional sample gives rise to surface dipole moments on its one-dimensional edges as well as to uncompensated charges on the zero-dimensional corners, see Fig. 1b. The former is indicating *gapped edge modes* while the latter motivates the presence of *in-gap corner excitations*. This also defines the key technological use of such a quadrupole insulator in mechanical or optical metamaterials: In two dimensions, the localized corner modes can be used to sense signals in the bulk which are then exponentially enhanced towards the corners, where they can be measured efficiently.[16] In three dimensions, the corner modes translate into one-dimensional modes which can be used to shuttle energy in a topologically protected way[17–20] between two points in space, useful for quantum information processing.[21]

The phenomenology of gapped edges and gapless corners can be formalized mathematically. Benalcazar et al.[1] proposed to use nested Wilson loops as a way to obtain a quantized quadrupole moment (see App. A): Wilson loop operators depend only on the bulk properties and encode the edge physics via their eigenvalues $\nu^{\pm}(k_\alpha)$, $\alpha = x, y$, known as Wannier bands.[22] If the Wannier bands $\nu^{\pm}(k_\alpha)$ are gapped, the eigenvectors of the Wilson loops can be used to define the bulk-induced edge polarization $p_\alpha^{\pm}$. In the same way as for the conventional topological insulators,[7] symmetries are required for the quantization of $p_\alpha^{\pm}$. It turns out that non-commuting mirror symmetries M_x and M_y lead to $p_\alpha^{\pm} \in \{0, 1/2\}$. In particular, the sought after quantized quadrupole phase is described by[1]

$$(p_x^{\pm}, p_y^{\pm}) = (1/2, 1/2). \tag{1}$$

As a corner terminates two edges, $(p_x^{\pm}, p_y^{\pm}) = (1/2, 1/2)$ could suggest that each of them supports two in-gap states. However, it is an important hall-mark of the bulk nature of the quadrupole insulator that each corner hosts only one mode, cf. Fig. 1b.[1]

A concrete tight-binding model for a two-dimensional quantized quadrupole insulator is shown in Fig. 1c.[1] The dimerized hopping with amplitude λ and γ leads to a band-gap between two pairs of degenerate bands for $\lambda \neq \gamma$ (see App. B). The black (red) lines in Fig. 1c indicate positive (negative) hoppings, effectively emulating a magnetic π-flux per plaquette. This π-flux requires the mirror-symmetry around the horizontal axis (M_y) to be accompanied by a gauge-transformation, leading to the non-commutation of M_x and M_y. The present model also has C_4 rotational symmetry (again up to a gauge-transformation) forcing $p_x^{\pm} = p_y^{\pm}$ as well as particle hole-symmetry giving rise to the aforementioned double degeneracy of the Bloch bands. For $\gamma < \lambda$ the topological phase $(p_x^{\pm}, p_y^{\pm}) = (1/2, 1/2)$, whereas for $\gamma > \lambda$, the trivial phase $(0, 0)$ is realized.[1] Here, we seek a mechanical implementation of a quadrupole insulator with $\ddot{x}_i = -\mathcal{D}_{ij} x_j$, where

the dynamical matrix $\mathcal{D}_{ij}$ couples local degrees of freedom x_i according to the model in Fig. 1c. Note that in the absence of a Pauli-principle, the notion of "filled bands" has to be replaced by "bands below the gap of interest."[23–25]

We implement the quadrupole insulator using the concept of perturbative mechanical metamaterials.[26] The starting point is a single-crystal silicon plate with dimensions $10{\times}10{\times}0.7$ mm, whose mechanical eigenmodes are described by the displacement field $\mathbf{u}(\mathbf{r})$. We work with the first non-solid-body mode which is characterized by two perpendicular nodal lines in the out-of-plane component of $\mathbf{u}(\mathbf{r})$, see Fig. 1d and Fig. 2a. By spectrally separating this mode from the modes below and above it, one can describe the dynamics in some frequency range by specifying only the amplitude x_i of the mode of interest of a given plate i. The hopping elements in $\mathcal{D}_{ij}$ are then implemented by thin beams between neighboring plates. The nodal structure of the mode allows to mediate couplings of either positive or negative sign, depending on which sides of the nodal lines are connected by the beams.
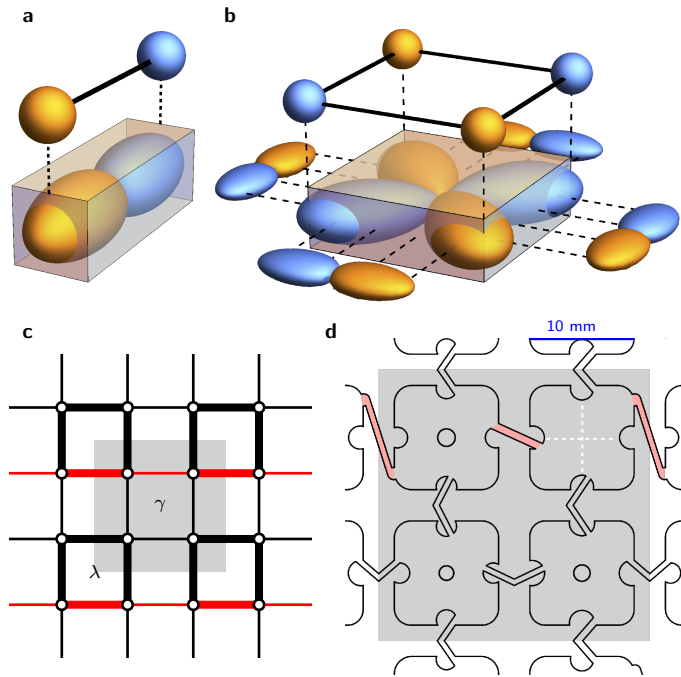

FIG. 1: **Quadrupole topological insulator a,** in a finite size system, a bulk dipole moment induces surface charges as illustrated by the spheres. **b,** A bulk quadrupole moment with its accompanying edge dipoles and corner charges. **c,** a concrete model for a system with a non-vanishing quadrupole moment. Thin (thick) lines denote weak (strong) hoppings with strength γ and λ respectively. The red (black) lines indicate a negative (positive) hopping amplitude resulting in a π-flux per plaquette. **d,** metamaterial design implementing the model in **c**. The out-of-plane plate-modes with two nodal lines (dashed white lines) are coupled via the bent beams. Beams connecting different sides of a nodal line (shaded red) mediate negative coupling matrix elements. The gray areas in **c** & **d** mark the unit cell of the tight-binding model.

Moreover, the distance to the nodal line controls the coupling strength mediated by a given beam. Combinatorial search[27] followed by a gradient optimization[26] leads to the design in Fig. 1d. Note that the rounded corners and the semi-circular exclusions guarantee spectral separation, cf. Fig. 2a, whereas the holes in the center adjust for plate-dependent frequency shifts induced by the beams. The beams are kinked to decrease their longitudinal stiffness ensuring spectral separation.

All measurements shown are performed using the same scheme: The plates are excited with an ultrasound air-transducer. The transducer has a diameter of 5 mm and is in close proximity to the sample, such that only a single plate is excited. We measure the response of the excited plate with a laser-interferometer. In this way, we measure the out-of-plane vibration amplitude $\Delta z_i \propto \psi_i^2$, where ψ_i is the eigenmode at the measured frequency. The inset of Fig. 2a shows the local mode of a single plate measured in this way. In all other figures we display the mechanical energy $\varepsilon_i \propto \Delta z_i^2$.

To identify the in-gap states we take a measurement of $\varepsilon_i(\nu)$ as a function of frequency ν on all plates i. We then apply the filters $\varepsilon_\alpha(\nu) = \sum_i \varepsilon_i(\nu) F_{i,\alpha}$ shown in Fig. 2d to separate the response of the bulk, edges, and corners. Figs. 2b & e show the resulting spectra for two different samples (see App. C). In the topologically trivial case with $\gamma > \lambda$, one can observe two frequency bands where the system absorbs energy (the theoretically predicted location of the bands is indicated in gray). Two features characterize this trivial phase: (i) No frequency range is dominated by the edge or corner response. Moreover, the relative weight of the three curves is in good accordance with the respective number of sites in the bulk, edges, and corners, respectively. (ii) No resonances appear in the gap between 36.0 kHz and 36.7 kHz. For the sample with $\gamma < \lambda$ in Fig. 2e, two key-features of the quantized quadrupole phase appear: (ii) close to 36.0 kHz and 36.7 kHz, the response is dominated by the edges, indicative of the bulk-induced gapped edge modes. (ii) Sharp resonances at the corners appear in the gap region. A small mirror symmetry breaking leads to the non-degeneracy of the in-gap states which we discuss below.

The spectra in Fig. 2b & e allow to identify three frequency regions $\mathcal{B}$, $\mathcal{E}$, and $\mathcal{C}$, where the bulk (blue), edge (orange), or corner (green) response dominates. To establish the quadrupole nature of the metamaterial, we analyze the site-dependent, frequency integrated response $\varepsilon_i^\alpha = \sum_{\nu \in \alpha} \varepsilon_i(\nu)$ with $\alpha = \mathcal{B}, \mathcal{E}, \mathcal{C}$. In Fig. 3a–c we show the resulting spatial profiles. Note that the bulk induces gapped edge-modes on all four sides of the sample.

The hallmark of the quadrupole phase lies in the counting of corner modes: Each corner terminates two-gapped edges, nevertheless, they all host only one in-gap mode.[1] In Fig. 3d, we show the response $\varepsilon(\nu)$ for the four corner plates. The resonances in the four plates are split by the imperfect termination and the disorder induced by the fabrication. However, each corner hosts only one resonance peak. Given the imperfection of our setup, where disor-
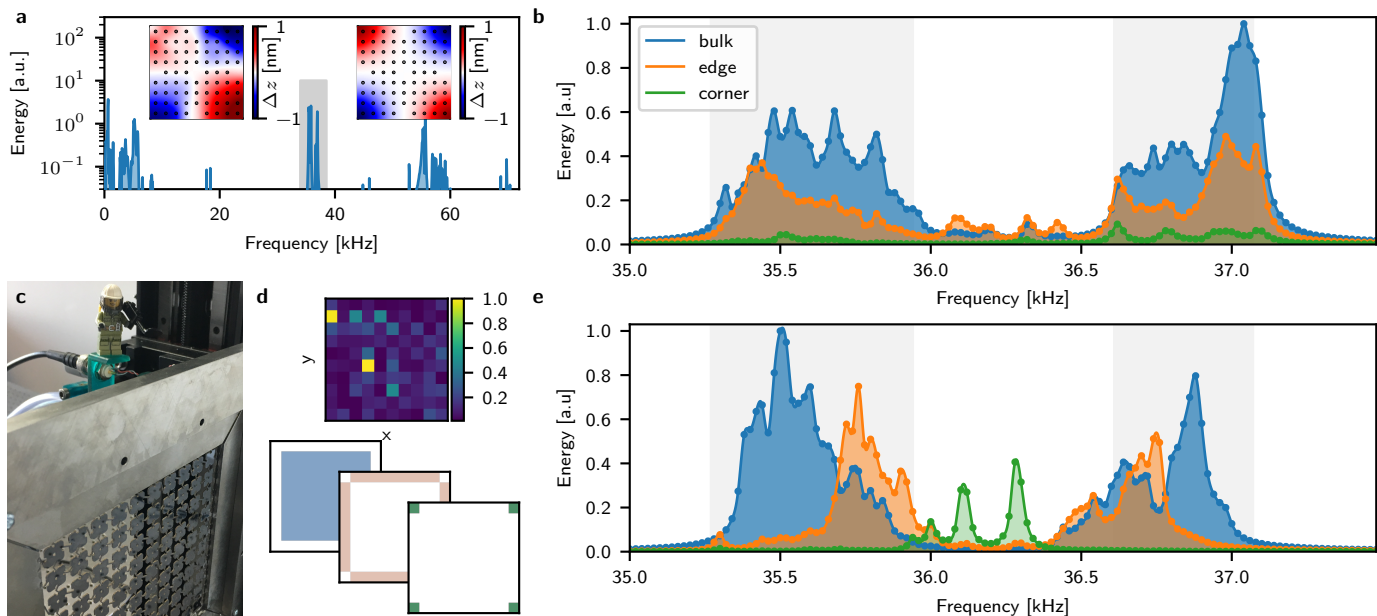
FIG. 2: **Quadrupole in-gap states a,** Spectrum on a single plate indicating the large separation between the targeted mode around 36 kHz (shaded gray) and the bands above and below. The left inset shows the mode profile measured on a single plate (the black dots mark the measurement points used for the interpolation), whereas the right inset shows the numerically calculated mode profile. In **d,** the response of all plates at an arbitrary frequency (37.0 kHz) is shown. These images are then multiplied by the displayed filters to determine bulk, edge, and corner response. **b** and **e** show the resulting spectra for the trivial and non-trivial sample, respectively. For the trivial case, one can see two bands (the gray area indicates the theoretically predicated location of the two bands) and a central gap with no resonances. For all frequencies, the weights of the bulk (blue), edge (orange), and corner (green) responses follow their fraction of the total 10x10 system. The non-trivial case (**e**) shows bulk- and edge-dominated frequency-regions and strong corner peaks in the middle of the gap. **c,** Photo of the setup.

der would generically split multiple mode per plate, this is only compatible with the mode-counting of a quadrupole insulator.

To corroborate our claim of observing a quadrupole insulator, we further explore the phase diagram of Ref. 1. When the C_4-symmetry is broken by allowing for different hoppings in x- and y-direction (see App. B), the phase $(p_x^\pm, p_y^\pm) = (1/2, 0)$ can be reached via a gap-closing of the surface modes. The $(1/2, 0)$-phase is characterized by gapped edge spectra on two parallel edges and no emergent edge physics on the perpendicular surfaces.[1] Moreover, the induced edge modes are in a trivial state and no corner charges are induced. In Fig. 3e, we show measurements on a sample in the $(1/2, 0)$-phase, where no in-gap states appear and the frequency region dominated by the edges draws its weight from only two surfaces.

In addition to the experimental data presented above, we also validate our system through extensive numerical calculations. The design process for the sample shown in Fig. 1d requires a finite-element simulation of the displacement fields $\mathbf{u}_i(\mathbf{r})$ on four unit cells containing a total of 16 sites i. The modes obtained in this way can then be projected onto the basis of uncoupled plate-modes $\mathbf{u}_i^0(\mathbf{r})$. In this way a reduced order model $\tilde{\mathcal{D}}_{ij}$ in the frequency range of the modes $\mathbf{u}_i^0(\mathbf{r})$ is obtained.[26] In Fig. 4a, we show the resulting model extended to a 10×10 system. The nearest neighbor couplings indeed follow the blueprint

of the target model shown in Fig. 1d. However, spurious long-range couplings mediated by off-resonant admixing of other single-plate modes induce a certain amount of mirror-symmetry breaking. This is most notable in the y-direction, where negative next-to-nearest neighbor couplings are mapped to positive ones, which is not corrected for in the gauge-transformation in M_y.

The reduced order model $\tilde{\mathcal{D}}_{ij}$ can also be used to calculate the topological indices $(p_x^\pm, p_y^\pm)$. The gapped Wannier bands $\nu_x^\pm(k_y)$ and $\nu_y^\pm(k_x)$ are shown in Fig. 4b. Note that the M_x symmetry implies $\nu_x^+(k_y) + \nu_x^-(k_y) = 1/2$ and the same for $x \leftrightarrow y$.[1] The absence of an exact M_y symmetry indeed leads to a breaking of this rule. This is also reflected in the value of the polarizations

$$(p_x^+, p_x^-) = (0.50, 0.49), \tag{2}$$
$$(p_y^+, p_y^-) = (0.58, 0.56). \tag{3}$$

As expected from the structure of $\tilde{\mathcal{D}}_{ij}$ shown in Fig. 4a, the polarizations are not precisely quantized. However, the phenomenology of in-gap corner modes is still observed as the symmetry breaking terms do not lead to any gap-closing, neither on the edge nor in the bulk.

The results presented in this paper underline the power of perturbative metamaterials.[26] On one hand, we leveraged this technique to find a first implementation of a quantized quadrupole insulator, a new class of topological
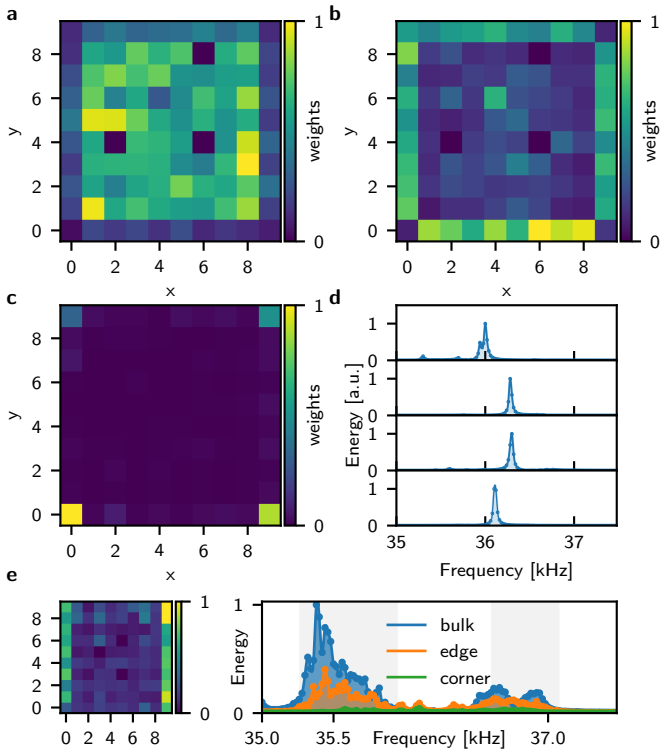
FIG. 3: **Edge and corner modes a – c,** Normalized integrated weights of the response of frequency regions in Fig. 1e where bulk (**a**), edge (**b**), and corner modes (**c**) dominate. **d,** Spectral response of the four corner sites in clock-wise arrangement starting from the top left corner. The combination of gapped edge modes on all four edges, see **b,** together with the single edge mode per site evidences the quadrupole nature of our metamaterial. **e,** Spectrum and edge dominated modes of a system in the non-quadrupole phase $(p_x, p_y) = (1/2, 0)$ showing no corner states but surface modes on two of the four edges.

materials. On the other hand, the platform of a continuous elastic medium provides a direct route to technological applications for any theoretical idea which can be represented by a tight-binding model.

Appendix A: Topological quantum number: Nested Wilson loops

Assuming two bands $n = 1, 2$ are filled, one can use the non-abelian Berry phase $\mathcal{A}^x_{nm}(\mathbf{k}) = i\langle u_m(\mathbf{k})|\partial_{k_x}|u_n(\mathbf{k})\rangle$ of the Bloch wave-functions $|u_n(\mathbf{k})\rangle$ to construct the Wilson-
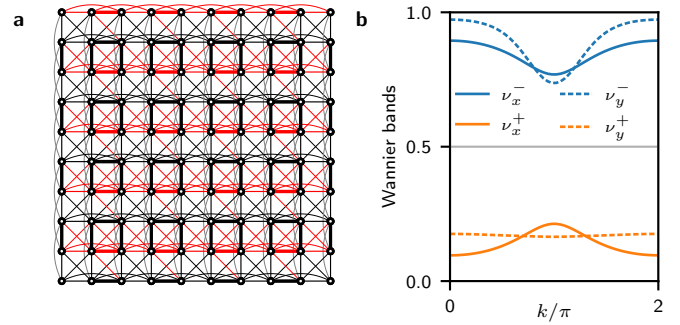

FIG. 4: **Reduced model and Wannier bands a,** Extracted reduced model for our design. Black (red) lines indicate positive (negative) couplings between the plate modes, whereas the thickness of the lines encodes the hopping amplitude. The unwanted next-to-nearest neighbor couplings arise from second-order effects involving other plate modes and break the M_x and M_y symmetries. **b,** Calculated Wannier bands from the model on the left.

loop operators

$$\mathcal{W}_x(k_y) = \mathrm{T}\exp\left[i\oint dk_x\,\mathcal{A}^x_{nm}(\mathbf{k})\right]. \qquad (A1)$$

Here, T denotes the path ordering along a closed loop in the Brillouin zone. The eigenvalues $\nu^\pm(k_y)$ of $\mathcal{W}_x(k_y)$ are in one-to-one correspondence to the spectrum of an edge perpendicular to the x-coordinate[22] (or perpendicular to y when x and y are interchanged). If the edge modes are gapped, the eigenvectors $v^\pm_n(k_y)$ of $\mathcal{W}_x(k_y)$ can be used to split the filled bands in a well-defined way: $|w_\pm(\mathbf{k})\rangle = \sum_{n=1}^2 v^\pm_n(k_y)|u_n(\mathbf{k})\rangle$. The nested polarization is then defined as

$$p_y^\pm = \frac{1}{(2\pi)^2}\int d\mathbf{k}\,\mathcal{A}^y_\pm(\mathbf{k}), \qquad (A2)$$

with $\mathcal{A}^y_\pm(\mathbf{k}) = i\langle w_\pm(\mathbf{k})|\partial_{k_y}|w_\pm(\mathbf{k})\rangle$. It can be shown that the presences of two mirror-symmetries M_x and M_y that do not commute are a necessary requirement for the nested polarizations $p_x^\pm$ and $p_y^\pm$ to be quantized to 0 or $1/2$.[1]

Appendix B: Model

The model shown in Fig. 1 can be expressed with the help of Γ-matrices $\Gamma_k = -\tau_2\sigma_k$, $\Gamma_4 = \tau_1\sigma_0$, $k = 1, 2, 3$; τ, σ are the standard Pauli-matrices. Using these matrices we can write[1]

$$\mathcal{D}(k_x, k_y) = [\gamma_x + \lambda_x\cos(k_x)]\Gamma_4 + \lambda_x\sin(k_x)\Gamma_3$$

$$+ [\gamma_y + \lambda_y\cos(k_y)]\Gamma_2 + \lambda_y\sin(k_y)\Gamma_1 = \sum_{i=1}^4 d_i(\mathbf{k})\Gamma_i. \qquad (B1)$$

The C_4-symmetric version of Fig. 1 is obtained by setting $\lambda_x = \lambda_y$ and $\gamma_x = \gamma_y$. The mirror symmetries
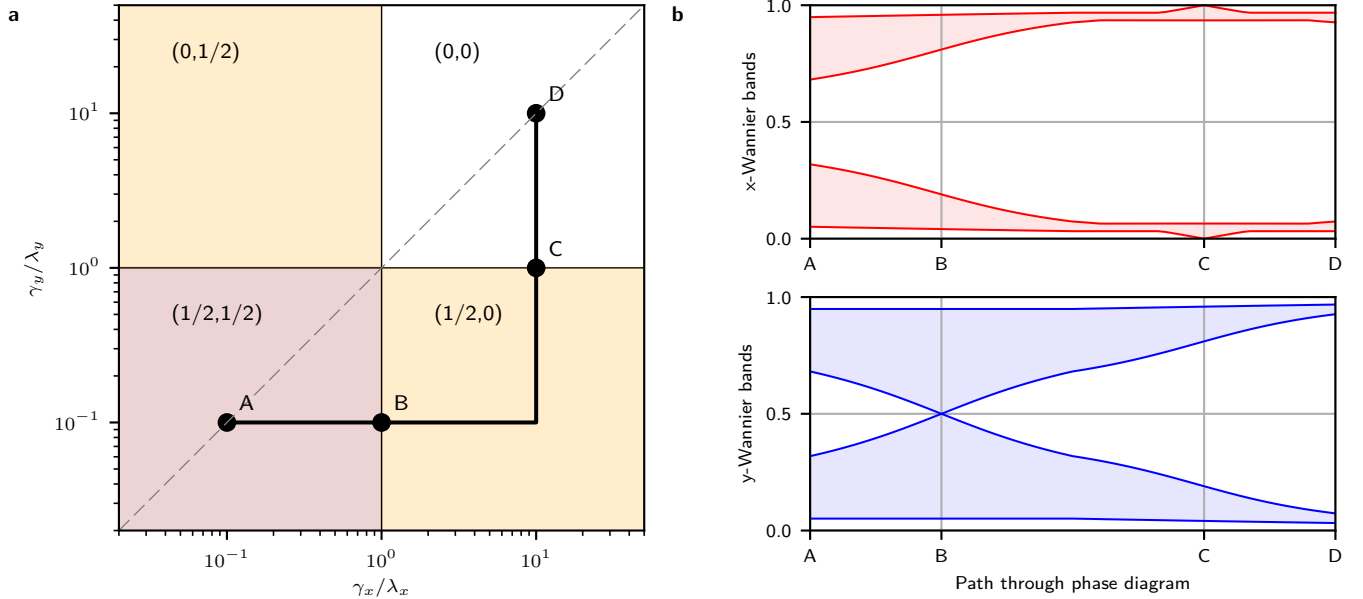
FIG. 5: **Phase diagram. a,** Phase diagram of model (B1). The brown area marks the quantized quadrupole phase, whereas the orange areas are the $(1/2,0)$ and $(0,1/2)$ phases with no corner modes but emergent edge physics along two parallel edges. The dashed lines indictes the C_4-symmetric line, where the bulk gap is closing at the phase transition. The transitions away from the C_4-symmetric line happen through bulk-induced edge-transitions, where no bulk gap is closing. **b,** The evolution of the Wannier bands in x and y direction along the path shown in **a**. The transition from the quadrupole phase to the $(1/2,0)$ phase is marked by a gap-closing at $1/2$, removing any polarization in the system. The second transition is induced by a gap closing at 0.

are represented by $\mathcal{D}(-k_x, k_y) = m_x \mathcal{D}(k_x, k_y) m_x^\dagger$ and $\mathcal{D}(k_x, -k_y) = m_y \mathcal{D}(k_x, k_y) m_y^\dagger$ with $m_x = \tau_1 \sigma_3$ and $m_y = \tau_1 \sigma_1$, respectively. The eigenvalues of $\mathcal{D}(k_x, k_y)$ are given by $\zeta = \pm |\mathbf{d}(\mathbf{k})|$, leading to two doubly-degenerate bands. Bulk gap-closings occur when $\mathbf{d}(\mathbf{k}) = 0$, which only happens for the C_4-symmetric case at $\lambda = \pm\gamma$. The spectrum of the mechanical system is given by $\nu = \sqrt{\nu_0^2 + \zeta}$, with a frequency offset ν_0. Finally, the eigenvectors $|u_n(\mathbf{k})\rangle$ of $\mathcal{D}(k_x, k_y)$ can be used to calculate the Wilson loop operators of Eq. (A1). The phase diagram and the evolution of the Wannier bands of model (B1) are shown in the extended data Fig. 5.

Appendix C: Sample design and preparation

The plate and beam geometry of Fig. 1d implement the sought after weak and strong, positive and negative coupling matrix elements. The definition of γ as the hopping strength *inside* a unit cell and λ *between* unit cells renders $\gamma < \lambda$ the non-trivial phase. Connected to this identification is the notion of how we are allowed to terminate the system: Surfaces have to be compatible with the unit-cells, i.e., are not allowed to cut through unit-cells. In turn, this also means we can use the same design of Fig. 1d and realize all phases shown in this paper by starting from a 10 ×10 sample in the $(1/2, 1/2)$-phase, then move the cut in y-direction by one row of sites to reach the $(1/2, 0)$-phase. Finally we move the termination one column and end up

in the $(0, 0)$-phase. The coupling matrix element are given by the ratio of the effective mass-density ρ_{eff} of the mode we use and the beam stiffness connecting two plates. We use a $700\,\mu m$ thick Si-wafer in [100] orientation, where we align the x- and y-axis of our model with the in-plane crystalline axes. The mass density of Si is $\rho = 2330\,\text{kg/m}^3$, the Young's moduli $E_x = E_y = E_z = 130\,\text{GPa}$, the Poisson ratios $\nu_{yz} = \nu_{zx} = \nu_{xy} = 0.28$, and the shear moduli $G_{yz} = G_{zx} = G_{xy} = 79.6\,\text{GPa}.$[28] This results in an offset frequency for our mode of $\nu_0 = 36.716 \pm 0.03\,\text{kHz}$ and the coupling matrix elements are given by $\lambda = 1.26 \pm 0.03 \times 10^9\,(\text{rad/s})^2$ and $\gamma = 0.43 \pm 0.01 \times 10^9\,(\text{rad/s})^2$. We produce our sample by laser-cutting with an accuracy of $\sim 50\,\mu m$, giving rise to the indicated uncertainties (disorder) in the coupling strengths. The wafers are clamped between two steel plates (each of $3\,\text{mm}$ thickness), cf. Fig. 2c. The impedance miss-match between the steel plates and the wafer leads essentially to fixed boundary conditions $\Delta z = 0$. The ultrasound air-transducer used was SMATR300H19XDA from Steiner & Martins Inc.

Appendix D: Signal analysis

Under the assumption that all modes have the same quality factor $Q \approx 1000$ (determined from the width of the corner modes), the completness of eigenmodes requires the integral $\int d\nu \, \Delta z_i(\nu) \propto \int d\nu \, \psi_i^2(\nu)$ to be the same for all sites i. We use this assumption to normalize all our

measurements in order to account for slight variations in the measurement points from site to site. In all figures where arbitrary units are indicated, we normalize to the maximal value shown in the respective figure. All measurements are subject to a systematic uncertainty of the interferometer of $\sim 5\,\mathrm{pm}$, and a statistical error determined by repeated measurements of $\sim 10\,\mathrm{pm}$, resulting in an error estimation on the displacements of $\sim 11.2\,\mathrm{pm}$. Careful error-propagation analysis results in error bars on all the figures which are smaller than the symbol size.

[*] These authors contributed equally to this work.

[1] W. A. Benalcazar, B. A. Bernevig, and T. L. Hughes, *Quantized Electric Multipole Insulators*, Science **357**, 61 (2017), URL.

[2] R. D. King-Smith and D. Vanderbilt, *Theory of polarization of crystalline solids*, Phys. Rev. B **47**, 1651(R) (1993), URL.

[3] M. Taherinejad, K. F. Garrity, and D. Vanderbilt, *Wannier center sheets in topological insulators*, Phys. Rev. B **89**, 115102 (2014), URL.

[4] M. V. Berry, *Quantal Phase Factors Accompanying Adiabatic Changes*, Proc. R. Soc. Lond. A **392**, 45 (1984), URL.

[5] K. v. Klitzing, G. Dorda, and M. Pepper, *New Method for High-Accuracy Determination of the Fine-Structure Constant Based on Quantized Hall Resistance*, Phys. Rev. Lett. **45**, 494 (1980), URL.

[6] D. J. Thouless, M. Kohmoto, M. Nightingale, and M. den Nijs, *Quantized Hall Conductance in a Two-Dimensional Periodic Potential*, Phys. Rev. Lett. **49**, 405 (1982), URL.

[7] C. L. Kane and E. J. Mele, Z_2 *Topological Order and the Quantum Spin Hall Effect*, Phys. Rev. Lett. **95**, 146802 (2005), URL.

[8] B. A. Bernevig, T. L. Hughes, and S.-C. Zhang, *Quantum Spin Hall Effect and Topological Phase Transition in HgTe Quantum Wells*, Science **15**, 1757 (2006), URL.

[9] L. Fu and C. L. Kane, *Time reversal polarization and a Z_2 adiabatic spin pump*, Phys. Rev. B **74**, 195312 (2006), URL.

[10] J. E. Moore and L. Balents, *Topological invariants of time-reversal-invariant band structures*, Phys. Rev. B **75**, 121306(R) (2007), URL.

[11] M. König, S. Wiedmann, C. Brüne, A. Roth, H. Buhman, L. W. Molenkamp, X.-L. Qi, and S.-C. Zhang, *Quantum Spin Hall Insulator State in HgTe Quantum Wells*, Science **318**, 766 (2007), URL.

[12] X.-L. Qi, T. L. Hughes, and S.-C. Zhang, *Topological field theory of time-reversal invariant insulators*, Phys. Rev. B **78**, 195424 (2008), URL.

[13] D. Hsieh, D. Qian, L. Wray, Y. Xia, Y. S. Hor, R. J. Cava, and M. Z. Hasan, *A topological Dirac insulator in a quantum spin Hall phase*, Nature **452**, 970 (2008), URL.

[14] C. K. Chiu, J. C. Y. Teo, A. P. Schnyder, and S. Ryu, *Classification of topological quantum matter with symmetries*, Rev. Mod. Phys. **88**, 035005 (2016), URL.

[15] S.-Y. Xu, I. Belopolski, N. Alidoust, M. Neupane, G. Bian, C. Zhang, R. Sankar, G. Chang, Z. Yuan, C.-C. Lee, et al., *Discovery of a Weyl fermion semimetal and topological Fermi arcs*, Science **349**, 6248 (2015), URL.

[16] M. Xiao, G. Ma, Z. Yang, P. Sheng, Z. Q. Zhang, and C. T. Chan, *Geometric phase and band inversion in periodic acoustic systems*, Nature Phys. **11**, 240 (2015), URL.

[17] S. D. Huber, *Topological mechanics*, Nature Phys. **12**, 621 (2016), URL.

[18] M. C. Rechtsman, J. M. Zeuner, Y. Plotnikm, Y. Lumer, D. Podolsky, F. Dreisow, S. Nolte, M. Segev, and A. Szameit, *Photonic Floquet topological insulators*, Nature **496**, 196 (2013), URL.

[19] M. Hafezi, S. Mittal, J. Fan, A. Migdall, and J. M. Taylor, *Imaging topological edge states in silicon photonics*, Nature Photon. **7**, 1001 (2013), URL.

[20] Z. Liu, X. Zhang, Y. Mao, Y. Y. Zhu, Z. Yang, C. T. Chan, and P. Sheng, *Locally Resonant Sonic Materials*, Science **289**, 1734 (2000), URL.

[21] N. Lang and H. P. Büchler, *Topological networks for quantum communication between distant qubits*, arXiv:1705.06901 (2017), URL.

[22] L. Fidkowski, T. S. Jackson, and I. Klich, *Model Characterization of Gapless Edge Modes of Topological Insulators Using Intermediate Brillouin-Zone Functions*, Phys. Rev. Lett. **107**, 036601 (2011), URL.

[23] R. Süsstrunk and S. D. Huber, *Observation of phononic helical edge states in a mechanical topological insulator*, Science **349**, 47 (2015), URL.

[24] R. Süsstrunk and S. D. Huber, *Classification of topological phonons in linear mechanical metamaterials*, Proc. Natl. Acad. Sci. USA **113**, E4767 (2016), URL.

[25] L. M. Nash, D. Kleckner, A. Read, V. Vitelli, A. M. Turner, and W. T. M. Irvine, *Topological mechanics of gyroscopic metamaterials*, Proc. Natl. Acad. Sci. USA **112**, 14495 (2015), URL.

[26] K. H. Matlack, M. Serra-Garcia, A. Palermo, S. D. Huber, and C. Daraio, *Designing Perturbative Metamaterials from Discrete Models: From Veselago lenses to topological insulators*, arXiv:1612.02362 (2016), URL.

[27] C. Coulais, E. Teomy, K. de Reus, Y. Shokef, and M. van Hecke, *Combinatorial design of textured mechanical metamaterials*, Nature **535**, 529 (2016), URL.

[28] J. J. Hall, *Electronic Effects in the Elastic Constants of n-Type Silicon*, Phys. Rev. **161**, 756 (1967), URL.